A RANS Solver Using a 3D Unstructured FVM Procedure

Hao ZHANG[*], Hajime NAKAGAWA, Taisuke ISHIGAKI[**] and Yasunori MUTO

[*]Graduate School of Engineering, Kyoto University
[**]Dept. of Civil & Environmental Engineering, Kansai University

Synopsis

　　A three-dimensional unstructured mesh based Reynolds-Averaged Navier-Stokes equation solver is presented with a Finite Volume Method. A strict but effective data structure is introduced to store the control volume information resulted from different meshing strategies. The power law scheme is adopted for the spatial discretization, and the implicit Crank-Nicolson scheme is employed for the temporal integral. In order to avoid the checkerboard phenomenon, the surface fluxes are calculated from the Rhie-Chow interpolation. The final algebraic equation system is solved using a preconditioned GMRES solver incorporated with an ILUTP preconditioner. The proposed solver has been applied to three kinds of turbulent flows in laboratorial flumes. It is found that the solver is able to reproduce the selected flows in different domains with a reasonable accuracy and manifests a potential to apply to the actual river conditions.

Keywords: Three-dimensional, FVM, unstructured mesh, k-ε model

1. Introduction

　　The two most commonly adopted meshing strategies in CFD (Computational fluid dynamics) community are generally referred to as structured mesh and unstructured mesh. The signature feature of structured mesh is the implicit grid structure, which may alleviate the need to store the mesh connectivity and permit the construction of rapid solution algorithms (Mavriplis, 1996). In order to take full advantages of structured mesh, many researchers have been devoting themselves to improving existing algorithms and developing new schemes. (e.g. Jongen, 1997; Kimura and Hosoda, 2003; Li and Fleming, 2003; Johnston and Liu, 2004; Brüger et al., 2005) However, despite its widespread use, the structured mesh methods are generally limited to solution domains of a relatively simple shape. It is very difficult and sometimes impossible to generate structured mesh for complex geometries, especially in 3D space. On the other hand, flows in complex geometries are usually encountered and of great interest in the engineering practices nowadays. For example, turbulent flows pass the natural rivers with extremely irregular cross sections or artificial channels with small but important hydraulic structures. An accurate resolution of the study domain and local mesh refinement necessitates the employment of unstructured mesh methods.

　　Although the past several decades have witnessed the significant development in unstructured mesh methods, most of the published literatures dealt with flow phenomena in other fields such as aerodynamics. (e.g. Mavriplis, 1997; Nakahashi et al., 1999; Hassan et al., 2000; Nakahashi et al., 2003; Basara, 2004) Hydraulic engineering poses many special problems requiring solution methods probably not included in other fields. But the related research is quite few to the authors' knowledge and is generally confined to 2D flows. For instance, Kim et al. (1997) reported a RANS (Reynolds-averaged Navier-Stokes equation) solver based on a 2D unstructured mesh, and the solver was

verified to be capable of predicting some wall-bounded turbulent flows with a good accuracy. Nallapati and Perot (2000) developed a staggered unstructured mesh method for the 2D calculation of free surface flows and it was applied successfully to some benchmark problems. Recently, Olsen (2003) constructed a 3D model to calculate the formation of a meandering channel. The turbulent flow was predicted with an unstructured mesh based k-ε model. Unfortunately, very few information has been shown on the quantitative comparison between the computational result and the physical model measurement in the paper. Haque et al. (2005) also carried out a 3D numerical simulation with a RANS solver provided by the commercial software FLUENT. The hybrid mesh adopted in the study was argued to be able to resolve the detailed hydraulic structures with a relatively small total number of cells. They compared the temperature distribution within a dam and its forebay situated on the Colombia River and found a reasonable similarity between the calculation and measurement. But the velocity field was not validated due to the shortage of field data.

In this study, an unstructured mesh based RANS solver is proposed based on a 3D FVM (Finite volume method) procedure. The standard k-ε model and some non-linear k-ε model have been integrated with this solver. The wall function approach is employed to resolve the near-wall area. Hybrid polyhedral mesh up to six faces may be used. This solver is designed as a module in a morphological model and may serve as a powerful tool for the investigation of river engineering.

The paper is organized as follows. In the succeeding section, a set of governing equations is firstly introduced. After that comes the detailed information on FVM formulation in Section 3. From Section 4 to Section 6, the discretization methods, the boundary conditions and the solution algorithms for sparse equation systems are presented one after another. In Section 7, three numerical examples are tested and computational results are compared with existing laboratorial measurements, which is followed by the final conclusion in Section 8.

2.   Governing equations

An engineer is usually concerned with the time-averaged properties of turbulences (Launder and Spalding, 1972). This suggests ways of accounting for the turbulences on the mean flow behavior by solving the RANS rather than solving the NS (Navier-Stokes equation) directly. In hydraulic engineering, as is well-known, the k-ε model and its variants are the widely used turbulence models based on the RANS. In this kind of models, the mean quantities are directly solved from the corresponding transport equations and the time-averaged turbulences are modeled by introducing some assumptions and simplifications.

2.1 Mean flow

The unsteady 3D RANS and continuity equation expressed in a Cartesian coordinate system with the tensor notation are as follows.

$$\frac{\partial u_i}{\partial t}+u_j\frac{\partial u_i}{\partial x_j}=f_i-\frac{1}{\rho}\frac{\partial p}{\partial x_i}+v\frac{\partial^2 u_i}{\partial x_j\partial x_j}+\frac{1}{\rho}\frac{\partial \tau_{ij}}{\partial x_j} \qquad (1)$$

$$\frac{\partial u_i}{\partial x_i}=0 \qquad (2)$$

where u_i= time-averaged velocity; x_i= Cartesian coordinate component; ρ = density of the fluid; f_i= body force; p= time-averaged pressure; v= molecular kinematic viscosity of the fluid; $\tau_{ij}=-\rho\overline{u_i'u_j'}$, are the Reynolds stress tensors, and u_i' is the fluctuating velocity component. The equation system is not closed, and the Reynolds stress tensors have to be evaluated in some other ways.

2.2 Turbulence closure

In the standard k-ε model, the Reynolds tensors are acquired through the linear constitutive equation.

$$-\overline{u_i'u_j'}=2v_t S_{ij}-\frac{2}{3}k\delta_{ij} \qquad (3)$$

where k= turbulence kinetic energy; δ_{ij} = the Kronecker delta; v_t = eddy viscosity and S_{ij}= the strain-rate tensor, the latter three are expressed by

$$\delta_{ij}=\begin{cases}1 & if \quad i=j \\ 0 & if \quad i\neq j\end{cases}$$

$$v_t=C_\mu\frac{k^2}{\varepsilon} \qquad (4)$$

$$S_{ij}=\frac{1}{2}\left(\frac{\partial u_i}{\partial x_j}+\frac{\partial u_j}{\partial x_i}\right)$$

in which C_μ is a coefficient, and is usually set to be a

constant and equal to 0.09, ε is the dissipation rate of the turbulence kinetic energy k. Two transport equations as described below are employed to estimate k and ε, respectively.

$$\frac{\partial k}{\partial t}+u_j\frac{\partial k}{\partial x_j}=\frac{\partial}{\partial x_j}\left[\left(v+\frac{v_t}{\sigma_k}\right)\frac{\partial k}{\partial x_j}\right]+G-\varepsilon \qquad (5)$$

$$\frac{\partial \varepsilon}{\partial t}+u_j\frac{\partial \varepsilon}{\partial x_j}=\frac{\partial}{\partial x_j}\left[\left(v+\frac{v_t}{\sigma_\varepsilon}\right)\frac{\partial \varepsilon}{\partial x_j}\right]+\left(C_{1\varepsilon}G-C_{2\varepsilon}\varepsilon\right)\frac{\varepsilon}{k} \quad (6)$$

where $G=$ the rate-of-production of the turbulence kinetic energy k, is defined as

$$G=-\overline{u_i'u_j'}\frac{\partial u_i}{\partial x_j} \qquad (7)$$

and the model constants suggested by Rodi (1980) generally take the universal values as below.

$$\sigma_k=1.0 \quad \sigma_\varepsilon=1.3 \quad C_{1\varepsilon}=1.44 \quad C_{2\varepsilon}=1.92 \qquad (8)$$

The standard k-ε model suffers from some inherent defects in particular the omission of any anisotropic eddy viscosity effects. This may be partially cured by introducing a non-linear constitutive relation between the turbulence stresses and the mean strain rate satisfying certain tensorial properties. Efforts and achievements have been make by many research groups such as Rubinstein and Barton, 1990; Gatski and Speziale, 1993; Shih et al, 1995 and Kimura and Hosoda, 2003. A general form for a quadratic constitutive equation can be summarized as

$$\overline{u_i'u_j'}=\frac{2}{3}k\delta_{ij}-2v_tS_{ij}$$
$$+a_1\frac{k^3}{\varepsilon^2}\left(\frac{\partial u_i}{\partial x_l}\frac{\partial u_l}{\partial x_j}+\frac{\partial u_j}{\partial x_l}\frac{\partial u_l}{\partial x_i}-\frac{2}{3}\frac{\partial u_k}{\partial x_m}\frac{\partial u_m}{\partial x_k}\delta_{ij}\right)$$
$$+a_2\frac{k^3}{\varepsilon^2}\left(\frac{\partial u_i}{\partial x_l}\frac{\partial u_j}{\partial x_l}-\frac{1}{3}\frac{\partial u_m}{\partial x_k}\frac{\partial u_m}{\partial x_k}\delta_{ij}\right) \qquad (9)$$
$$+a_3\frac{k^3}{\varepsilon^2}\left(\frac{\partial u_l}{\partial x_i}\frac{\partial u_l}{\partial x_j}-\frac{1}{3}\frac{\partial u_m}{\partial x_k}\frac{\partial u_m}{\partial x_k}\delta_{ij}\right)$$

where a_1, a_2 and a_3 are coefficients, which may have different values due to different models.

3.   Finite volume formulation

In an FVM procedure, the study domain is divided into a number of continuous polyhedral CVs (Control volumes). If one integrates the governing PDEs (Partial differential equations) over a CV, the general form reads

$$\frac{\partial}{\partial t}\int_V \phi\, dV+\int_S \phi u\cdot n dS=\int_S \Gamma\nabla\phi\cdot n dS+\int_V b dV \qquad (10)$$

where $V=$ the volume of the CV; $S=$ the CV surface with a unit normal vector n directing outwards; $\phi=$ general conserved quantity representing either scalars or vector and tensor field components; $u=$ the fluid velocity vector whose Cartesian components are u_i or (u, v, w); $\Gamma=$ diffusion coefficient and $b=$ the volumetric source of the quantity ϕ. It is noted that Eq. 10 has a left side of a transient term and a convective term balanced by a diffusive term and a source term on the right. The equation is mesh-independent and is valid for arbitrary polyhedral CVs. As a result, an FVM procedure is able to take full advantages of an unstructured mesh system. Moreover, summation of the equations for all CVs leads to the global conservation equation because the inner CV faces will cancel out. This is also one of the most attractive points to use FVM in engineering practices.

3.1 Data structure

In an unstructured mesh method, the mesh connectivity is not implicitly known. Since the CVs may be numbered in any order and have any number of neighbors, an extra space in the memory should be maintained for that kind of information. This may sometimes result in a considerable consumption of computer resources.

As is known, any kind of polyhedral mesh may be used in the simulation theoretically, but the generally adopted unstructured mesh in engineering practices is confined to tetrahedra, pyramids, prisms and hexahedra. A partial explanation lies in the difficulty of generating polyhedral mesh with more than six faces. Amongst all the above mesh types, the hexahedron may be accounted as the general case, and the quadrilateral is the general case for the CV face correspondingly. It indicates that a hybrid mesh system in practice is possible to be considered as a hexahedral mesh provided that the polyhedra with less than six faces are assigned some nominal ones to satisfy the convention. This provides a way to simplify the data structure in storage.

In order to define the connectivity of the CVs, there are a lot of alternatives. The most general data structure
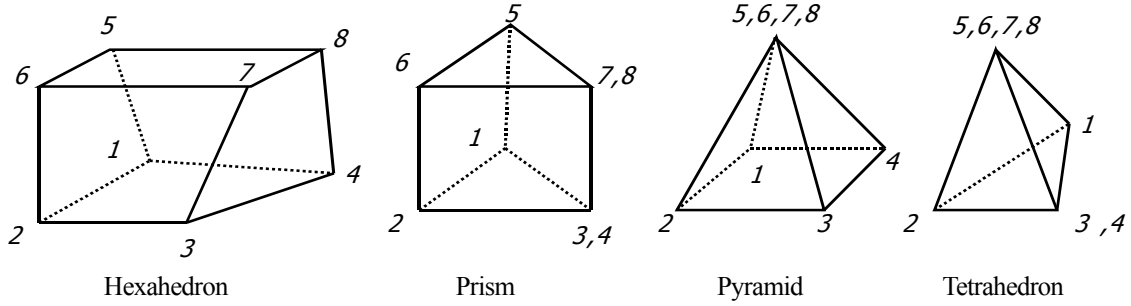
Fig.1 CV and its vertices

contains all the information of the CV explicitly. That is: a CV is defined by its six faces, faces by the lists of edges and edges by their corresponding vertices. However this method is not preferred to reduce the number of arrays needed for the definition of mesh connectivity. A simplified data structure is introduced here. This method is also employed in some CFD codes and recommended by Ferziger and Perić (2002).

As indicated in Fig. 1, the CV is defined by a list of its eight vertices in a counter-clockwise order. With such definition, the faces enclosing the CV and the edges forming the faces are also uniquely identified. They may be implicitly organized in an ordered way without occupying any computer memory. Moreover, since the arbitrary polyhedral mesh is stored as a hexahedral mesh, the number of the neighboring CVs is fixed to be six. Hence the neighboring CV which shares a common face with the current CV may also be indexed in the same ordered way as that for the faces. For nominal hexahedra, due to the existence of nominal faces, some of the vertices will be repeated during storing as also shown in Fig. 1. Using this kind of treatment, the input of the mesh system includes only a list of nodal coordinates, a list of vertices of the CVs and a list of the neighboring CVs.

3.2 Surface and volume calculation

With the aforementioned data structure, it is no need to evaluate the geometrical elements for arbitrary polyhedra. The calculation is limited to quadrilaterals in 2D and hexahedra in 3D. As the area and the center of a triangle is very easy to acquire. One can subdivide a quadrilateral face into two triangles and the vector area is approximated by the summation of those of the two sub-triangles. For instance, the vector area of the quadrilateral (1,2,3,4) in Fig. 2 is computed from

$$r_i = x_i \mathbf{i} + y_i \mathbf{j} + z_i \mathbf{k} \tag{11}$$

$$S_{1234} = S_{123} + S_{134} =$$
$$\frac{1}{2}\left[(r_2 - r_1) \times (r_3 - r_1) + (r_3 - r_1) \times (r_4 - r_1)\right] \tag{12}$$

where r_i = the ith vertex of the CV; $\mathbf{i, j, k}$ = unit vectors in the x, y, z coordinate directions; S_{123}, S_{134} = vector areas of the sub-triangles Δ_{123} and Δ_{134}, respectively and S_{1234} = vector area of the quadrilateral surface (1,2,3,4).

The center of the surface is the mean value of those of the sub-triangles weighted by the corresponding area, i.e.

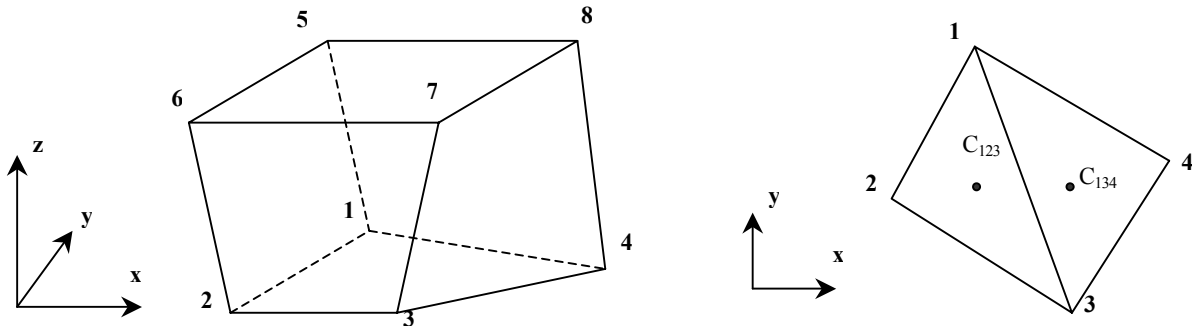$$\mathbf{c}_{1234} = \frac{S_{123}\mathbf{c}_{123} + S_{134}\mathbf{c}_{134}}{S_{1234}} \tag{13}$$

Fig.2 Surface and volume calculation

where c= the center of a surface and S= the area of a surface.

Extending the above logic from 2D to 3D, a hexahedron is divided into 6 tetrahedra. The evaluation of the volume is thus acquired by summation of the volumes of all the sub-tetrahedra corresponding to their partitioning. And the volume of a tetrahedron is a dot product of two vectors, for example the volume of tetrahedron (1,5,6,7) is

$$V_{1567} = \frac{1}{3}(\mathbf{r}_5 - \mathbf{r}_1) \cdot \mathbf{S}_{567} \qquad (14)$$

where V_{1567}= the volume of tetrahedron (1,5,6,7). The centroid of the CV is the mean value of those of the sub-tetrahedra weighted by the corresponding volume.

$$\mathbf{c}_V = \frac{\sum V_i \mathbf{c}_i}{V} \qquad (15)$$

where $\mathbf{c}_V$= the centroid of the CV; V_i= the volume of sub-tetrahedron i (i ranges from 1 to 6) and $\mathbf{c}_i$= the centroid of sub-tetrahedron i.

According the above analysis, the sub-routine for the calculation of the geometry elements can be easily coded.

4. Discretization methods

In a collocated FVM procedure, the variables are defined at the center of the CV. A second order midpoint rule is generally used for the integral approximation. If the transient term is absent for the time being, the control volume equation (i.e. Eq. 10) may be discretized term by term and written as

$$\sum_f \phi_f \left(u_{f\perp} S_f \right) = \sum_f \Gamma_f \frac{\partial \phi}{\partial n} \bigg|_f S_f + b_P - s_P \phi_P \qquad (16)$$

where $u_{f\perp}$= the fluid velocity normal to the surface; b_P= part of the source term containing all the contributions excluding unknown variables and $-s_p \phi_p$ = part of the source term including the unknown variables which can be treated implicitly. The subscript P= the present CV and the subscript f= the face of the CV.

It is readily seen that Eq. 16 is not an explicit expression of the variables defined at the centers of the CVs. Values at other locations have to be obtained by some kind of interpolation methods. The diffusive term contains the gradient of a quantity, which necessitates some numerical differentiation techniques.

An arithmetic interpolation method is commonly used to evaluate the surface values. For a quantity ϕ on the surface,

$$\phi_f = \alpha_f \phi_P + (1 - \alpha_f)\phi_A \qquad (17)$$

where $\alpha_f = \dfrac{d_{Af}}{d_{Af} + d_{fP}} \qquad (18)$

in which the subscript A= the adjacent CV, d_{fP} and d_{Af} are the distances from the surface to the present CV and to the adjacent CV, respectively. If the line connecting the two CV centers does not pass through the center of the common face center, a correction term may be introduced. In this case

$$\phi_f = \phi_{f'} + (\nabla \phi)_{f'} \cdot (\mathbf{r}_f - \mathbf{r}_{f'}) \qquad (19)$$

where f'= the intersection of the surface and the line connecting the two neighboring CVs (see Fig. 3), the gradient at f' is obtained by interpolating the cell-center gradients at either side of the face. And the Gauss' theorem may be employed to determine the cell-center gradients.
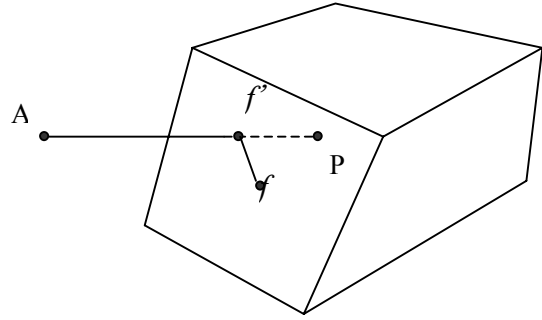

Fig.3 Interpolation of the surface value

The discretization methods adopted here have been suggested by some other publications such as Ferziger and Perić (2002) and applied to various problems. It serves as a basic scheme whenever a surface quantity needs to be interpolated.

4.1 Spatial discretization

From the viewpoint of stability and ease of programming, higher order scheme is avoided in this study. The power law scheme is employed during the spatial discretization. This scheme is relatively easy and has been confirmed to be applicable in 3D calculations (Wilson et al., 2003; Olsen, 2004).

With the power law scheme, Eq. 16 can be finally

assembled as

$$\sum_f \left\{ \left[D_f A\left(\left|P_f\right|\right) + \max\left(-F_f, 0\right) \right]\left(\phi_P - \phi_A\right) + F_f \phi_P \right\} = b_P - s_P \phi_P \qquad (20)$$

where the strength of the convection F_f, diffusion conductance D_f and the ratio of them are given as

$$F_f = u_{f\perp} S_f, \quad D_f = \frac{\Gamma_f S_f}{d_{AP}}, \quad P_f = \frac{F_f}{D_f} \qquad (21)$$

and

$$A\left(\left|P_f\right|\right) = \max\left[0, \left(1 - 0.1\left|P_f\right|\right)^5\right] \qquad (22)$$

The interpolation of the diffusive coefficient on the surface and the surface flux deserve special attention. For the diffusive coefficient, the harmonic mean may reflect more physics and reasonableness in particular near the boundary. This results in

$$\Gamma_f = \frac{\Gamma_A \Gamma_P}{\alpha_f \Gamma_P + \left(1 - \alpha_f\right)\Gamma_A} \qquad (23)$$

A simple arithmetic mean for the surface flux may lead to checkerboard variable distribution, which has caused the slow acceptance of the use of collocated mesh. This problem can be cured by the interpolation method proposed by Rhie and Chow (1983). The method introduces an additional term related to the pressure gradient when calculating the fluxes on the surface.

As is known, the unknown quantities of the present CV can be finally expressed by all of its neighboring CVs after discretization. For instance, the momentum equations for u at present CV and one of its adjacent CVs are written as

$$a_P u_P = \sum_{nb} a_{nb} u_{nb}\big|_P - \int_V \frac{\partial p}{\partial x} dV\big|_P + b_P$$
$$a_A u_A = \sum_{nb} a_{nb} u_{nb}\big|_A - \int_V \frac{\partial p}{\partial x} dV\big|_A + b_A \qquad (24)$$

where a= coefficient for the unknown at the center of the approximated CV and nb= the neighboring CV.

From the conservation principle of the FVM formulation, the velocity at the common face of the two neighboring CVs must also have a discretized momentum equation of the similar form as that of Eq.24, i.e.

$$a_f u_f = \sum_{nb} a_{nb} u_{nb}\big|_f - \int_V \frac{\partial p}{\partial x} dV\big|_f + b_f \qquad (25)$$

Approximating the solution u_f of Eq.25, the information from Eq.24 can be used. By using some linear interpolation and simplification, the following equation is obtained.

$$u_f = \bar{u}_f + \frac{1}{a_f}\left(\overline{\int_V \frac{\partial p}{\partial x} dV}\big|_f - \int_V \frac{\partial p}{\partial x} dV\big|_f\right) \qquad (26)$$

where

$$\bar{u}_f = \alpha_f u_P + \left(1 - \alpha_f\right)u_A$$
$$a_f = \alpha_f a_P + \left(1 - \alpha_f\right)a_A$$
$$\overline{\int_V \frac{\partial p}{\partial x} dV}\big|_f = \alpha_f \int_V \frac{\partial p}{\partial x} dV\big|_P + \left(1 - \alpha_f\right)\int_V \frac{\partial p}{\partial x} dV\big|_A \qquad (27)$$
$$\int_V \frac{\partial p}{\partial x} dV\big|_f = S_{fx}\left(p_A - p_P\right)$$

in which S_{fx}= projected area of the surface to the yz plane (perpendicular to the x axis). The extension to other velocity components is straightforward.

4.2 Temporal integral

At the end of the spatial discretization, one can get

$$\frac{\partial}{\partial t}\int_V \phi dV = F \qquad (28)$$

where $F = \sum_{nb} a_{nb}\phi_{nb} + b_P - a_P\phi_P$

Taking the second order implicit Crank-Nicolson scheme as follows

$$\frac{\phi^{m+1} - \phi^m}{\Delta t}V = \frac{F^{m+1} + F^m}{2} \qquad (29)$$

where the superscript m and $m+1$ stand for the previous and the current time step. One can arrive at the final algebraic equation set.

$$a_P \phi_P^{m+1} = \sum_{nb} a_{nb}\phi^{m+1} + b_P \qquad (30)$$

in which

$$a_P^{m+1} = \sum_{nb} a_{nb}^{m+1} + \sum_f F_f + s_P^{m+1}$$
$$a_P = a_P^{m+1} + \frac{2V}{\Delta t} \qquad (31)$$
$$b_P = b_P^{m+1} + \frac{2V}{\Delta t}\phi_P^m + \left(\sum_{nb} a_{nb}\phi_{nb} + b_P - a_P\phi_P\right)^m$$

It is seen from Eq. 31 that after the time integral, a

time-related term is introduced to the coefficient of a_P comparing with the steady case. And besides a temporal term, there is another contribution from the previous time step to the source term.

4.3 Pressure-velocity coupling

The solution procedure follows the SIMPLE (Semi-implicit method for pressure-linked equations) algorithm. The main concept of this method is to guess the pressure and get a pressure correction with the continuity equation. The procedure is summarized here.

In the derivation, the guessed pressure and the velocity field not satisfying the continuity equation are denoted with an index *, the correction of the variable is denoted with an index ', and the variable without any superscript stands for the corrected value. Hence,

$$u_i = u_i^* + u_i'$$
$$p = p^* + p' \tag{32}$$

Extracting the pressure term from the source term in the discretized momentum equation, the velocity component in the x direction satisfies

$$a_P u_P^* = \sum_{nb} a_{nb} u_{nb}^* - \sum_f A_{fx} p_f^* + b_p \tag{33}$$

On the other hand, the same momentum equation based on the corrected velocity component has the following form

$$a_P u_P = \sum_{nb} a_{nb} u_{nb} - \sum_f A_{fx} p_f + b_p \tag{34}$$

If Eq. 33 is subtracted from Eq. 34 and Eq. 32 is taken into account, the velocity correction is obtained.

$$u_P' = \frac{\sum a_{nb} u_{nb}'}{a_P} - \frac{\sum A_{fx} P_f'}{a_P} \tag{35}$$

In a SIMPLE method, the first term on the right hand side is omitted. Then the velocity correction in the CV center has a simple relation with the pressure correction. For the velocity correction on the surface, the same relationship is assumed to be valid instead of interpolating the value from the CV centers. It means

$$u_f' = -\frac{1}{a_P} A_{fx} \left(P_A' - P_P' \right) \tag{36}$$

The correction of other velocity components may be derived in the same way. The corrected velocity field is

then introduced to ensure the continuity equation. An equation set for the pressure correction will be obtained.

$$\sum_f \left[\left(\sum_{i=x,y,z} u_{fi} A_{fi} \right) + \left(\sum_{i=x,y,z} \frac{A_{fi}^2}{a_{Pi}} \right) \left(P_P' - P_A' \right) \right] = 0 \tag{37}$$

This equation set is closed and solution of the equations yields the pressure correction. The velocity field is renewed and a new iteration starts until convergence.

5. Boundary conditions and near-wall treatment

Appropriate boundary conditions should be specified depending on the nature of the flow. The inlet boundary is generally considered as a Dirichlet boundary and all the quantities have to be prescribed. At the outlet boundary, the flow information is usually little known. A Neumann boundary with zero gradients may be assumed if the outlet is set as far downstream of the study domain as possible. The water surface is considered as a symmetrical plane for the time being. It may be acceptable for many hydraulic problems. Special attention has been paid for the impermeable wall boundaries.

The no-slip condition is the appropriate condition for velocity components at both the riverbed and the side-walls. However the wall function approach is preferred here to avoid the possible integration through the viscous sub-layer and implement the wall roughness more flexibly. In the wall function approach, the near wall CV velocity is assumed to be parallel to the wall and denoted by $u_{//}$. Although it is not always the case, the treatment can be simplified without significant influence on the result.

With the definition of the dimensionless distance y^+ and dimensionless velocity u^+ as follows

$$y^+ = \frac{u_* y_\perp}{\nu}, \quad u^+ = \frac{u_{//}}{u_*} \tag{38}$$

where u_* = the friction velocity near the bed and $y_\perp$ = the normal distance from the center of the near wall CV to the wall surface, the universal wall function can be expressed by

$$u^+ = \frac{1}{\kappa} \ln \left(E y^+ \right) \tag{39}$$

where κ = the van Karman constant (= 0.41) and E = roughness parameter of the wall. Assuming that the

flow is in local equilibrium, i.e. the production and dissipation rate of the turbulence are nearly equal, one can obtain

$$u_* = C_\mu^{1/4} k_P^{1/2} \tag{40}$$

Then the wall shear stress is written as

$$\tau_w = \rho u_*^2 = \frac{\rho C_\mu^{1/4} k_P^{1/2} u_{//}}{u^+} \tag{41}$$

In the momentum equations, the link with the wall is suppressed by setting it to zero and adding the wall force in Eq.41 as a source term. The normal derivative of k at the wall boundary CV is set to be zero in the k-ε equation, and the production in the wall region is computed from

$$G_P = \frac{\tau_w}{\rho} \frac{\partial u_{//}}{\partial n} = \frac{\tau_w}{\rho} \frac{u_{//}}{y_\perp} \tag{42}$$

ε in the near wall CV is directly set to

$$\varepsilon_P = \frac{u_*^3}{\kappa y_\perp} = \frac{C_\mu^{3/4} k_P^{3/2}}{\kappa y_\perp} \tag{43}$$

The roughness parameter in Eq. 39 provides a simple way to take the bed roughness into account. Suggested by some researchers (e.g. Wu et al., 2000; Salaheldin, 2004), this parameter may be evaluated as below.

$$E = \exp\left[\kappa\left(B - \Delta B\right)\right] \tag{44}$$

where B=5.2, is a constant; ΔB= roughness function defining the shift of the intercept due to roughness effect, it is evaluated from

$$\Delta B = \begin{cases} 0 & k_s^+ < 2.25 \\ B_m \sin\left[0.4285\left(\ln k_s^+ - 0.811\right)\right] & 2.25 \le k_s^+ < 90 \\ B_m & k_s^+ \ge 90 \end{cases} \tag{45}$$

in which

$$\begin{aligned} B_m &= B - 8.5 + \frac{\ln k_s^+}{\kappa} \\ k_s^+ &= \frac{u_* k_s}{v} \end{aligned} \tag{46}$$

and k_s is the equivalent roughness height. For a hydraulic smooth bed, k_s=0, and for a rough bed, many empirical relations are available in the literatures according to the bed conditions (e.g. Chang, 1988; van Rijn, 1993).

6. Solution methods

The equations are solved in an implicit decoupled way. The final algebraic equation systems are under-relaxed before submitted to the equation solver. The widely used method proposed by Patankar (1980) is adopted here. It has been found to be very efficient owing to its increasing of the diagonal dominance of the coefficient matrices.

Considering the sparseness and non-symmetry characteristic of the coefficient matrices, Krylov subspace iterative methods are preferred. The most popular and representative methods may include GMRES (Generalized minimal residual method), Bi-CGSTAB (Bi-conjugate gradient stabilized method) and TFQMR (Transpose-free variant of quasi-minimal residual method). In order to get practically useful, the iterative solver usually works with a suitable preconditioner. In this study, a preconditioned GMRES is employed together with an ILUTP (Incomplete LU factorization with threshold and pivoting) preconditioner. A complete presentation on iterative methods and preconditioning techniques can be found in the book published by Saad (2003).

7. Applications

The proposed methodology is applied to three kinds of turbulent flows in the following sub-sections. Different turbulence models and different meshing strategies have been tested.

7.1 Flow in a straight rectangular channel

Imamoto et al. (1987) carried out a series of experiments concerning the flow in open channels. An LDV (Laser Doppler velocimeter) system was used to measure the fully developed turbulent flow velocities in a transverse cross-section. In this section, one case was selected to verify the proposed methods.

Table 1 Experiment conditions

Width B(cm)	Depth H(cm)	Discharge Q(l/s)	Slope I_e	Reynolds number	Froude number
20.0	4.00	2.055	1/1,400	7,700	0.48

The experiment conditions are given in Table 1. The laboratory flume is geometrically symmetrical, and only half of the domain is calculated by employing a symmetrical plane boundary condition. A longitudinal
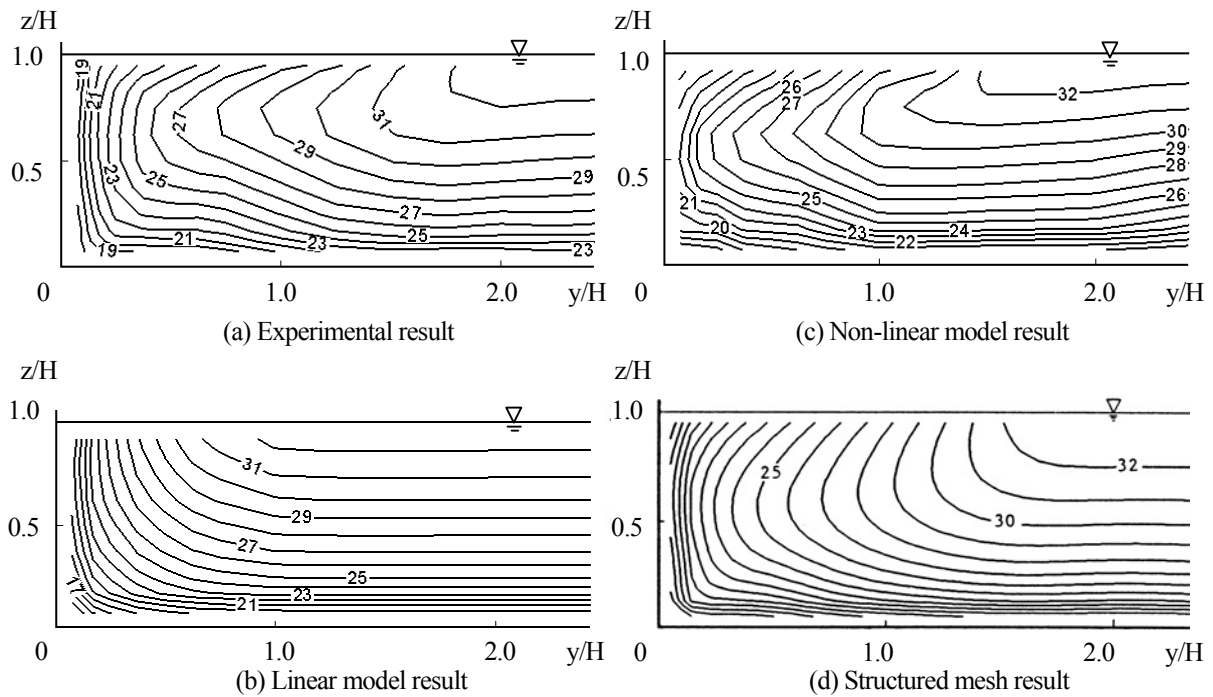
z/H

(a) Experimental result

z/H

(c) Non-linear model result

z/H

(b) Linear model result

z/H

(d) Structured mesh result

Fig. 4 Comparison of the longitudinal velocity u (cm/s)

distance of 140cm (=35H) is assumed to be long enough to diminish the influence of inlet and outlet boundaries and has been chosen for the simulation after some trial computations. The standard k-ε model and a non-linear k-ε model proposed by Kimura and Hosoda (2003) are implemented on a hexahedral mesh with a total number of 10,626, respectively. A logarithmic velocity profile is

prescribed at the inlet boundary. The turbulent quantities k and ε are specified corresponding to a viscosity ratio of 10.0 and taking the turbulence intensity 8%.

The computed longitudinal velocity and turbulence kinetic energy in the transverse cross-section compared with the experimental result are shown in Fig.4 and Fig.5, respectively. Ishigaki (1993) simulated the same flow

z/H

(a) Experimental result

z/H

(c) Non-linear model result

z/H

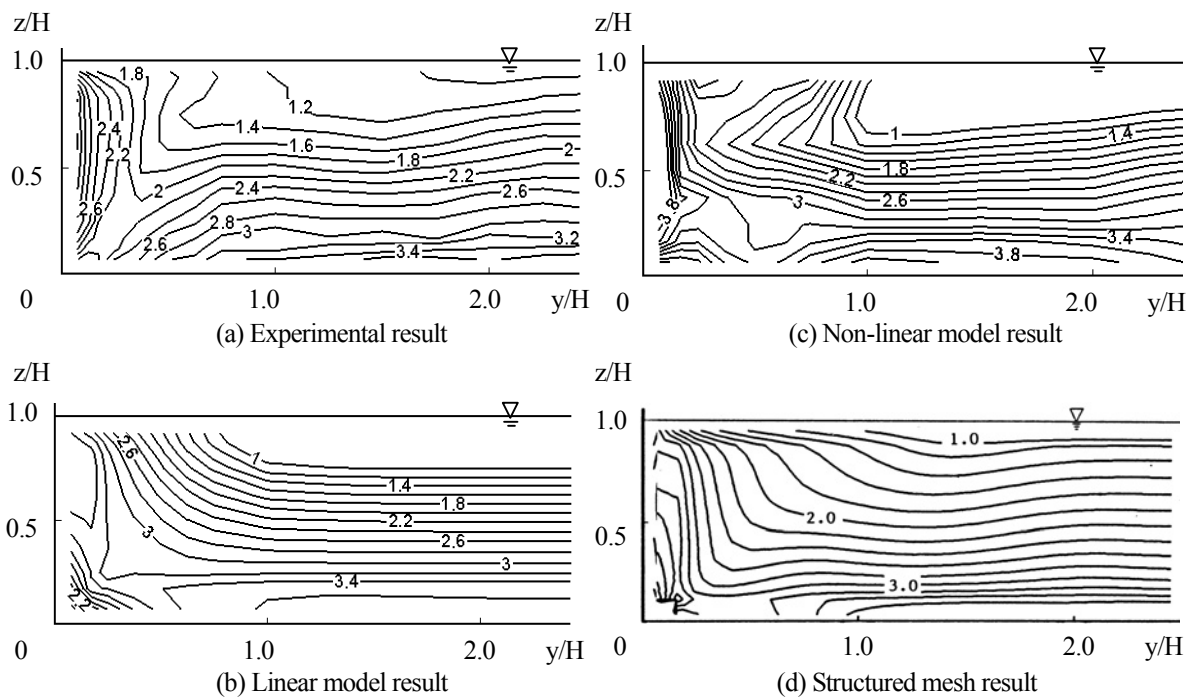(b) Linear model result

z/H

(d) Structured mesh result

Fig. 5 Comparison of turbulence kinetic energy normalized by squared friction velocity k/u_*^2

phenomenon with two ARS (Algebraic Reynolds stress simulation) models based on a structured mesh. The result of one of the models proposed by Naot and Rodi (1982) is also shown in the figures.

A standard model does not include any information of the vortices and the secondary currents, which in return affects the prediction of the mean flow pattern. This may be evidently observed in the comparison of the longitudinal velocity in Fig. 4. Both the non-linear model and the ARS model give a closer result to the LDV measurements than the linear one. It is also interesting to note that the non-linear model in this selected case seems to perform even better than the ARS model. The reason is not much known, but it demonstrates that the

unstructured mesh method in this study is at least comparable to a structured one.

In the comparison of the turbulence kinetic energy (the absolute value has been normalized by the squared friction velocity), the non-linear model again manifests itself to be the best solution. However, in all computational cases, the area near the wall boundaries has been slightly over-estimated. A further comparison is carried out in Fig. 6 between the experimental result and the non-linear model for the lateral Reynolds stress distribution at different water depths. The values are again normalized by the squared friction velocity. The over-estimation of the Reynolds stresses near the boundary area is observed. And away from the boundary,
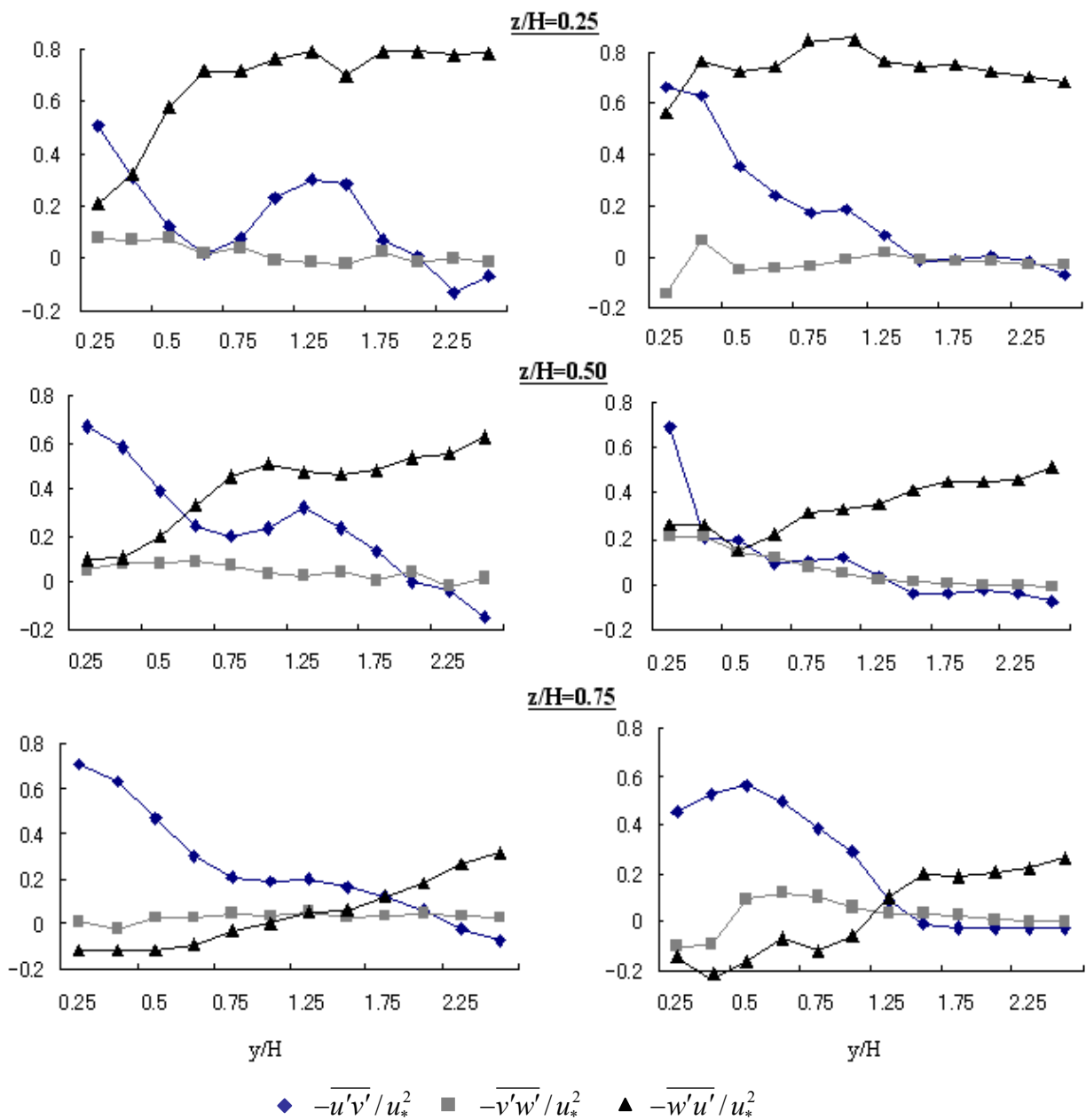

Fig. 6 Comparison of the lateral Reynolds stress distribution (Left: Experiment; Right: Computation)

the model result is very close to the measurements. The employment of the wall function approach may be the main error source for this simulation.

7.2 Flow in a square embayment

The flow in an embayment is one of the most important hydraulic phenomena in the river engineering practice. Due to the complex flow structure, the balance of the sediment transport is broken. It results in a great number of problems, for instance, the local scouring, the change of environmental parameters, etc. By using two LDAs (Laser Doppler anemometers) and an EMC (Electromagnetic current meter), Muto et al. (2000) experimentally investigated the flow exchanges between the main channel and an embayment area. In this section, the methodology is applied to one of this kind of flows and the result is compared with the measurements.
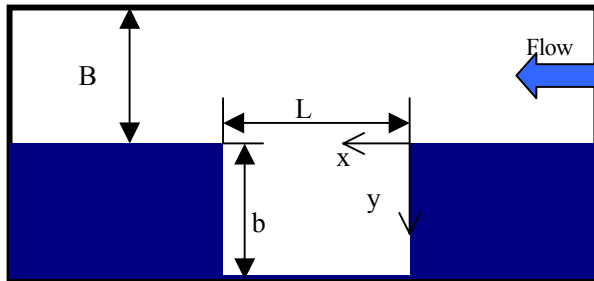
Fig.7 Top view of the experimental setup

The laboratory flume consists of a main channel which has a width B=16.0cm and a flood plain with a width b=16.0cm. Part of the flood plain is removed where forms an embayment with a length L=16.0cm. The experiment set up is shown in Fig. 7. And the experiment conditions are summarized in Table 2.

Table 2 Experiment conditions

Discharge Q (l/s)	Water depth H (cm)	Friction velocity u_*(cm/s)	Reynolds number	Froude number
2.271	3.8	2.055	9,650	0.74

In the computation, the inlet boundary is set at the distance of about $10b$ from the upstream of the embayment and the outlet is $20b$ from the downstream of the embayment. This distance seems long enough and may diminish the effect of the inlet and outlet boundaries. The inlet flow is assumed to have a logarithmic velocity

profile in the vertical direction. At the beginning of the calculation, this velocity profile is applied to the whole domain.

Two kinds of meshing strategies have been tested with a non-linear k-ε model under the same initial and boundary conditions. The mesh system near the embayment in either case is shown in Fig. 8 and Fig. 9, respectively.

Around the embayment, the mesh is clustered for a better resolution, and away from the embayment, the mesh is relatively coarse to save computational time. The hybrid mesh consists of both hexahedra and prisms having a total mesh number of 13,086. And the hexahedral mesh is a bit finer with a total number of 19,683.
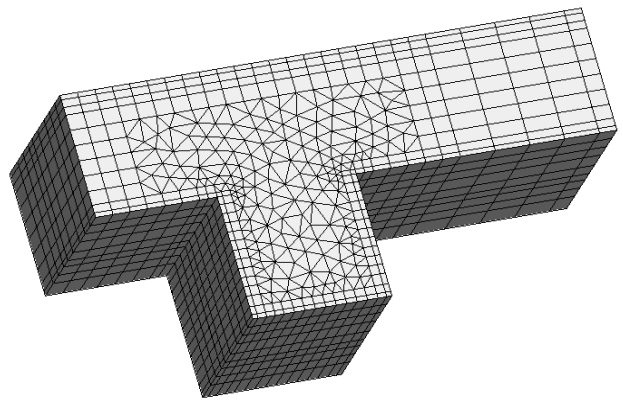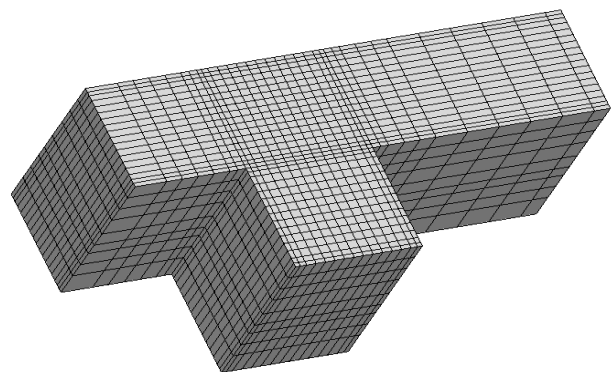

Fig.8 Hybrid mesh

Fig.9 Hexahedral mesh

The longitudinal velocity and the horizontal vortex at half water depth are shown in Fig. 10 and Fig. 11, respectively.

Both the hybrid mesh and the hexahedral mesh work well in this test case. The flow pattern in the embayment has been reproduced with a reasonable accuracy. A large
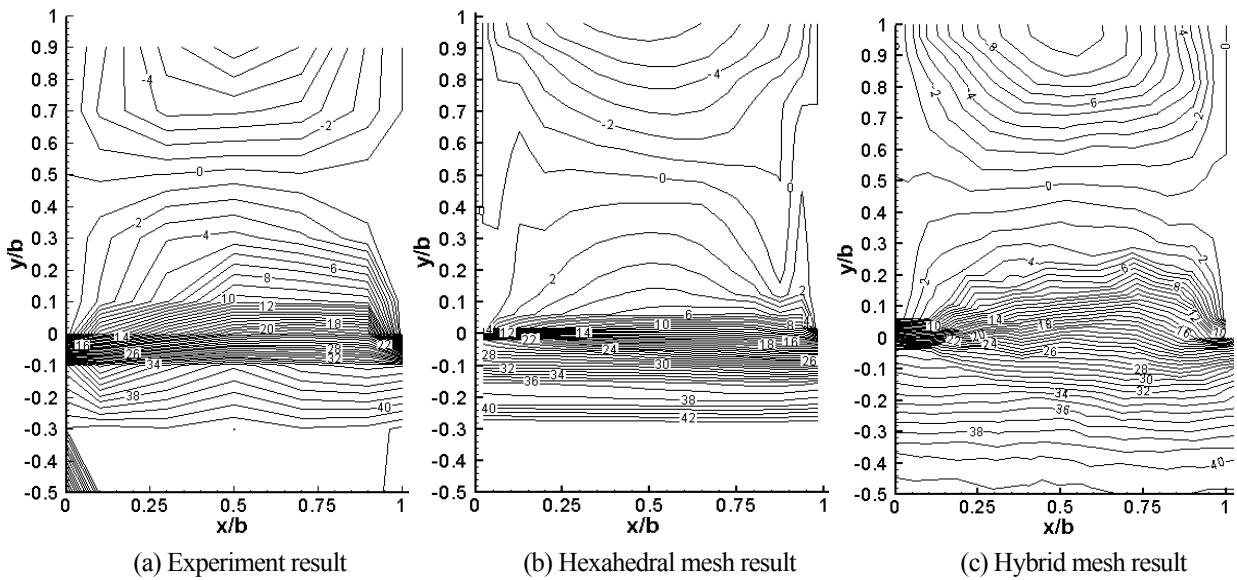
(a) Experiment result　　(b) Hexahedral mesh result　　(c) Hybrid mesh result

Fig. 10 Comparison of the longitudinal velocity profile

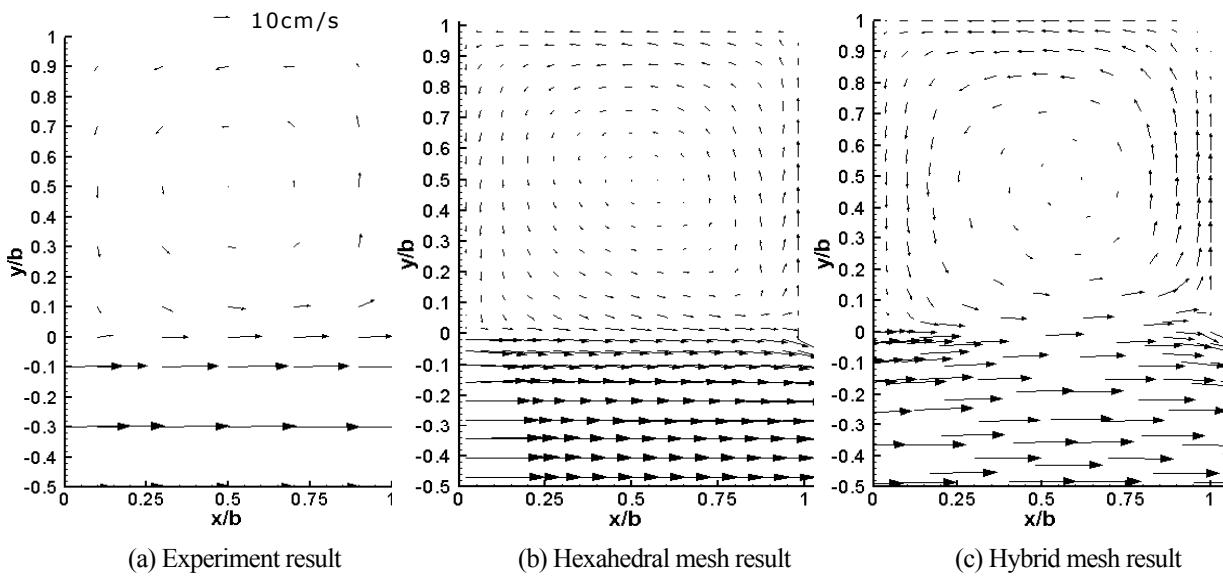(a) Experiment result　　(b) Hexahedral mesh result　　(c) Hybrid mesh result

Fig. 11 Comparison of the horizontal cross-sectional velocity profile (u, v)

circulating flow is induced in the embayment area as shown in Fig. 11. This circulation occupies almost the whole region of the embayment with a maximum velocity about a quarter of that in the main channel. At the center of the circulation, the flow is stagnant. Velocity gradients in the junction zone (i.e. the interface between the main channel and the embayment) are quite steep. Although there are some differences in the result due to the two different mesh systems, it is very difficult to distinguish the winner.

7.3 Flow around spur dykes with local scour holes

The final application is the prediction of the flow field around a series of impermeable spur dykes with
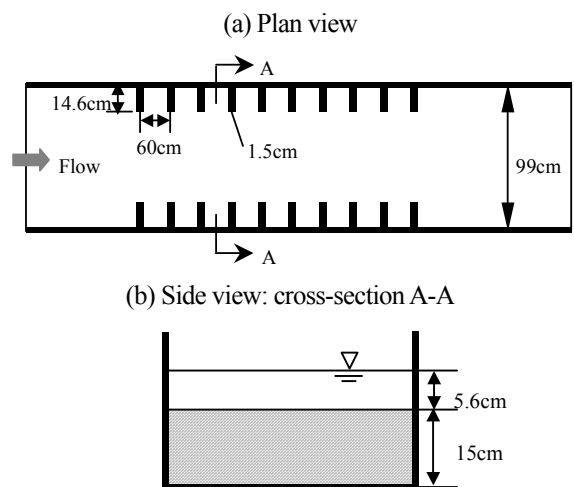
(a) Plan view

(b) Side view: cross-section A-A

Fig. 12 Experiment setup

Table 3 Experiment conditions

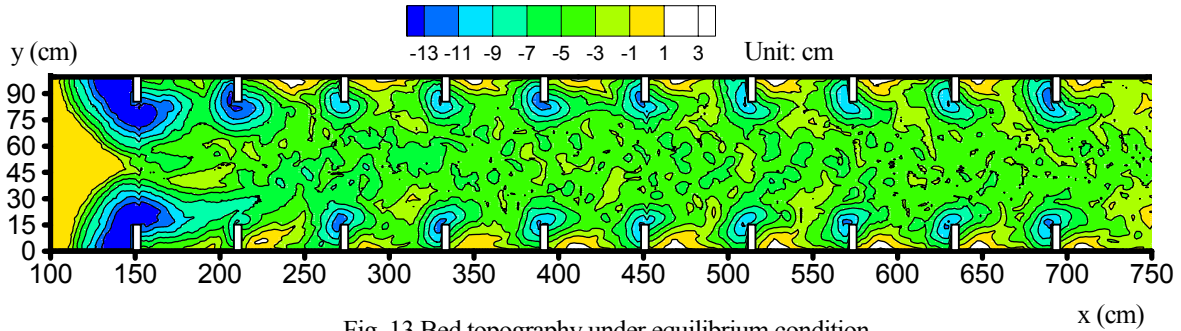| Discharge Q (l/s)	Mean velocity u (cm)	Slope I_e	Approach flow depth H (cm)	Shear velocity u_*(cm/s)	Shear velocity ratio (u_*/u_{*c})	Reynolds number	Froude number
10.52	18.98	1/3,000	5.60	1.35	0.915	10,682	0.26

Fig. 13 Bed topography under equilibrium condition

local scour holes. Detailed measurements were reported by Khaleduzzaman (2004) and Zhang et al. (2005). The experiment is conducted in a straight tilting flume, which is 20m long, 0.99m wide and 0.3m deep. The initial riverbed was covered with 15cm-thick fine sediment. The sediment has a mean diameter of 196 μm and a geometric standard deviation of 1.496.

The experiment setup and the experiment conditions are given in Fig. 12 and Table 3, respectively. It satisfies the condition of clear-water scouring. The final riverbed topography after a continuous running of 893 hours is shown in Fig. 13. Severe local scour holes are observed at the toes of all the spur dykes. Around the first pair, all the sediment has been eroded. The main channel area has

been significantly degraded, while along the channel bank, obvious deposition occurs. The 3D flow velocity in the equilibrium state is measured with an I-shape and an L-shape electromagnetic velocity meters under dynamic flow conditions. The average of 600 samples processed by a computerized data acquisition system at a frequency of 10Hz is taken as the time-averaged value of each measured quantity at each point.

The flow calculation is based on the final riverbed with a k-ε turbulence model. A hexahedral mesh system with a total number of 31,808 is employed for the calculation. Considering the geometrical symmetry, only half of the flume is selected as the computational domain.
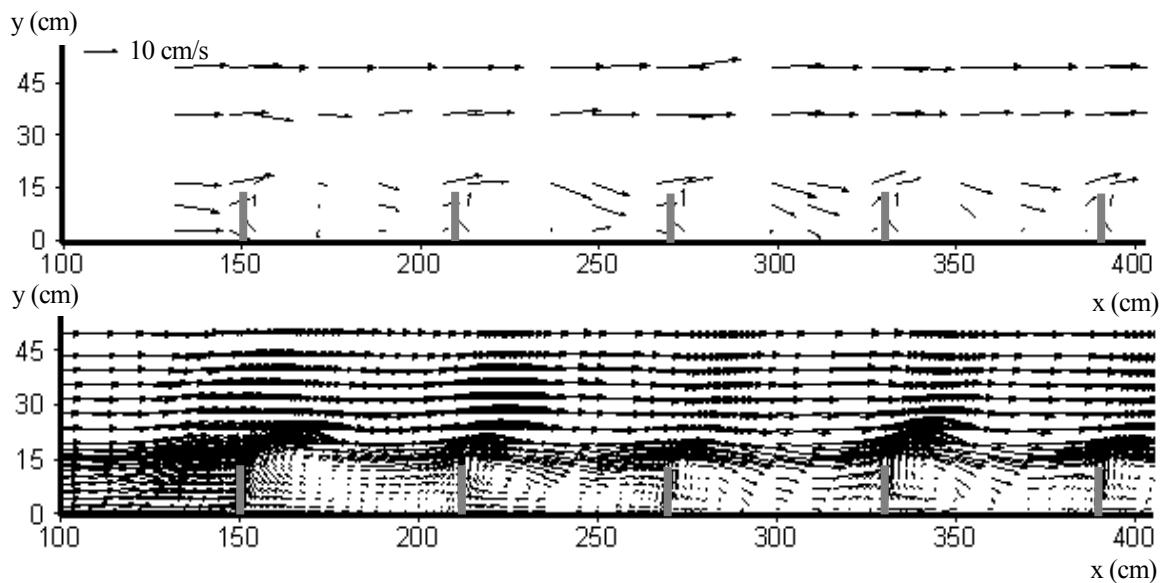

Fig. 14 Stream-wise velocity profile (u, v) around the first five spur dykes at z=1.0cm
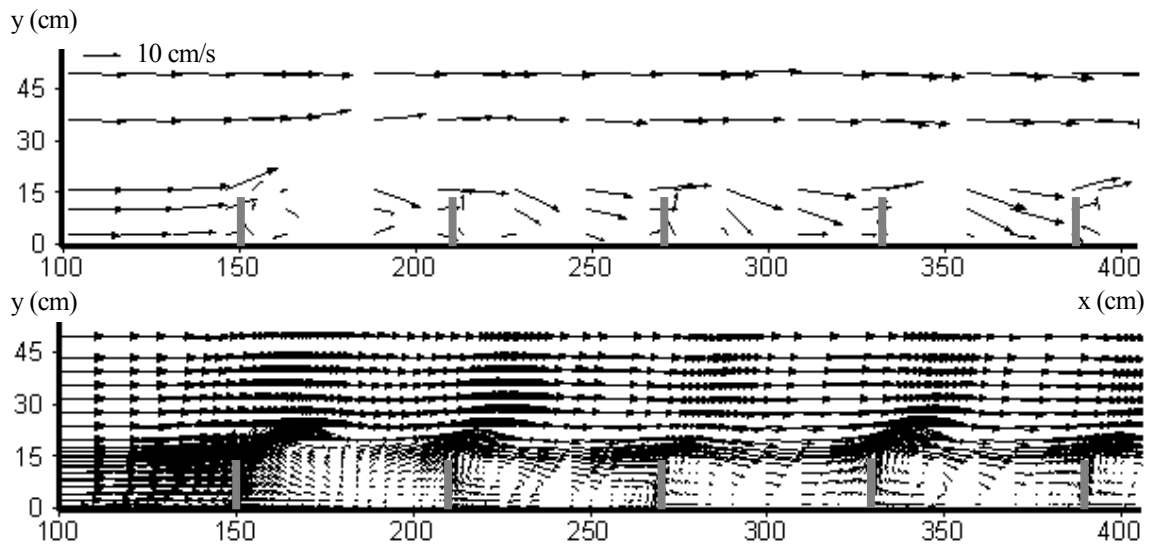(Experiment: top; Computation: bottom)

Fig. 15 Stream-wise velocity profile (*u, v*) around the first five spur dykes at *z*=3.25cm
(Experiment: top; Computation: bottom)

The stream-wise velocity profiles (*u, v*) around the first several spur dykes at two different layers (*z*=1.0cm and *z*=3.25cm) are shown in Fig. 14 and Fig. 15, respectively.

Although the magnitude of the velocity vector in the two layers is different, the flow pattern shows some similarity. The velocity diverts at the heads of the spur dykes. In the main channel area, the velocity is intensified, and there is a significant velocity reduction in the embayment areas formed by the consecutive spur dykes. Take a look at the experimental data, one may find that there is a wake vortex in each embayment area. The center of the vortex is closer to the upstream spur dyke forming the embayment area. This phenomenon has been reasonably reproduced by the computation.

A further inspection may lead to some more interesting discoveries. In the computational result, one may find a small eddy at the downstream corner of each embayment. These eddies are not found in the plot for the experimental data. This may be due to the shortage of enough measured data. If the data has been collected at more locations, the small eddies may be expected to appear. In fact, similar small eddies have been observed on the free surface during the surface flow visualization (Zhang et al., 2005). In the first embayment, the computed vortex system is a little different from the others, which coincides with the experiment measurements. The obvious 3D characteristics of the flow structure due to the local scour hole in this area may be responsible for this difference. As has mentioned before, the first spur dyke is surrounded by

the deepest scour hole. It has a great effect on the flow field.

In the junction zone, the measured velocity seems a bit larger than the computed one. This may be attributed
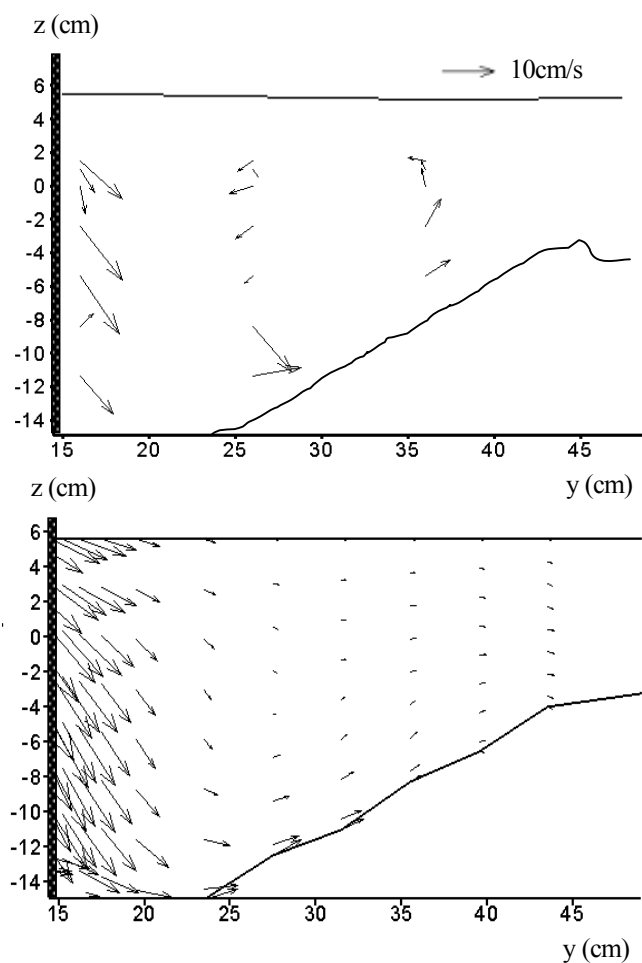

Fig. 16 Transverse velocity profile (*v, w*) at the head of the first spur dyke (Experiment: top; Computation: bottom)

to the coarse mesh adopted in the test case. As the velocity gradient in this area is quite deep, a finer mesh may be suggested for a better resolution.

A comparison of the transverse cross-sectional velocity profile (v, w) at the head of the first spur dyke (i.e. x=150.0cm) is depicted in Fig. 16 finally. This figure gives an intuitive image of the vertical flow pattern in the local scour hole. The basic aspects of the flow structure have been reasonably captured with the numerical simulation. The vertical velocity component w at the head of the spur dyke is quite large. A big anti-clockwise vortex occupies almost the whole scour area if one takes a look from the downstream. No wonder the sediment just in front of the spur dyke is completely eroded.

8. Conclusions

A 3D unstructured mesh based RANS solver using an FVM procedure has been presented in this paper. With a strict but simple data structure, the solver can take full advantages of arbitrary polyhedral mesh up to six faces. Special techniques distinguished from those of structured mesh methods have been accentuated including the discretization of the governing equations, the wall boundary treatments, etc.

The solver has been incorporated into different kinds of turbulence models and applied to flows in different domains with different meshing strategies. The comparison of the computational result and the experimental data demonstrates that the solver is able to reproduce the selected flows with a reasonable accuracy. Furthermore, the stableness, effectiveness and simplicity of the solver are also observed during the model verification. It may be accounted as a promising solution for the turbulence modeling in hydraulic engineering practices.

Nevertheless, some assumptions and simplifications have been introduced in the solver, which may become the bottleneck and limit the application of the proposed method. These include the omission of the water surface variation and the assumption made for the wall function approach. Moreover, higher order discretization schemes have been avoided in this study in order that the solver is as stable as possible. This may sometimes become the main error source for the simulation. All these problems should be taken into account in the future research.

References

Basara, B. (2004): Employment of the second-moment turbulence closure on arbitrary unstructured grids, International Journal for Numerical Methods in Fluids, Vol.44, pp.377-407.

Brüger, A., Gustafsson, B, Lötstedt, P. and Nilsson, J. (2005): High order accurate solution of the incompressible Navier-Stokes equations, Journal of Computational Fluids, Vol. 203, pp. 47-91.

Chang, H.H. (1988): Fluvial Processes in River Engineering, John Wiley & Sons, Inc.

Ferziger, J.H. and Peric, M. (2002): Computational Methods for Fluid Dynamics, 3rd rev. ed., Springer-Verlag.

Gatski, T.B. and Speziale, C.G. (1993): On explicit algebraic stress models for complex turbulent flows, Journal of Fluid Mechanics, Vol.254, pp.59-78.

Haque, M.D., Koken, M., Constantinescu, S.G. and Weber, L. (2005): Use of a 3D RANS model to predict stratification effects related to fish passage at hydropower dams, http://www.iihr.uiowa.edu/people/ resume/constantinescu/NEW_PAPERS_WEB/SEOUL _Haque.pdf

Hassan, O., Probert, E.J., Morgan, K. and Weatherill, N.P. (2000): Unsteady flow simulation using unstructured meshes, Computer Methods in Applied Mechanics and Engineering, Vol. 189, pp. 1247-1275

Imamoto, H., Ishigaki, T. and Kajima, A. (1987): Velocity vector measurement by Laser Doppler Velocimeter in an open channel flow (3), Annuals of Disas. Prev. Res. Inst., Kyoto Univ. No. 30 B (2), pp. 643-654. (in Japanese)

Ishigaki, T. (1993): Study on 3D Flow Structures in Compound Open Channels, Ph. D Thesis, Kyoto Univ. (in Japanese)

Johnston, H. and Liu, J.G. (2004): Accurate, stable and efficient Navier-Stokes solvers based on explicit treatment of the pressure term, Journal of Computational Physics, Vol. 199, pp. 221-259

Jongen, T. (1997): Simulation and Modeling of Turbulent Incompressible Fluid Flows, Ph. D Thesis, Swiss Federal Institute of Technology.

Khaleduzzaman, A.T.M. (2004): Experimental Study on River Course Stabilization and Restoration by Using Groin-like Structures, Master thesis, Kyoto Univ.

Kim, S. E., Mathur, S. R., Murthy, J. Y. and Choudhury, D. (1997): A Reynolds-averaged Navier-Stokes solver using an unstructured mesh based finite-volume scheme, Fluent Technical Notes, (TN117) Fluent, Inc.

Kimura, I. and Hosoda, T. (2003): A Non-linear k-ε Model with Realizability for Prediction of Flows around Bluff Bodies, International Journal for Numerical Methods in Fluids, Vol. 43, pp. 818-837.

Launder, B.E. and Spalding, D.B. (1972): Lectures in Mathematical Models of Turbulence, Academic Press.

Li, B. and Fleming, C.A. (2003): Three-dimensional hydrodynamic model for free surface flow, Journal of Hydraulic Research, IAHR, Vol.41, No.4, pp. 367-377.

Mavriplis, D.J. (1996): Mesh generation and adaptivity for complex geometries and flows, Handbook of Computational Fluid Mechanics, Peyret, R. (ed.), Academic Press, pp.417-459.

Mavriplis, D.J. (1997): Unstructured grid techniques, Annual Review of Fluid Mechanics, Vol. 29, pp. 473-514.

Muto, Y., Imamoto, H. and Ishigaki, T. (2002): Velocity measurements in a straight open channel with a rectangular embayment, Proc. of the 12th APD-IAHR, Bangkok, Thailand.

Naot, D. and Rodi, W. (1982): Calculation of secondary currents in channel flow, Journal of Hydraulics Division, Proc. ASCE, Vol. 108, pp. 948-968.

Nakahashi, K., Sharov, D., Kano, S. and Kodera, M. (1999): Applications of unstructured hybrid grid method to high-Reynolds number viscous flows, International Journal for Numerical Methods in Fluids, Vol. 31, pp. 97-111.

Nakahashi, K., Ito, Y. and Togashi, F. (2003): Some challenges of realistic flow simulations by unstructured grid CFD, International Journal for Numerical Methods in Fluids, Vol. 43, pp. 769-783.

Nallapati, R. and Perot, B.J. (2000) Numerical simulation of free-surface flows using a moving unstructured mesh, Proc. of ASME 2000 Fluids Engineering Division Summer Meeting, June 11-25, Boston, Massachusetts

Olsen, N.R.B. (2003): Three-dimensional CFD modeling of self-forming meandering channel, Journal of Hydraulic Engineering, ASCE, Vol. 129 (5), pp. 366-372.

Patankar, S.V. (1980): Numerical Heat Transfer and Fluid Flow, McGraw-Hill, New York.

Rhie, C.M. and Chow, W.L. (1983): Numerical study of the turbulent flow past an airfoil with trailing edge separation, Journal of AIAA, Vol. 21, pp. 1525-1532.

Rodi, W. (1980): Turbulence Models and Their Application in Hydraulics - a State of the Art Review, University of Karlsruhe, Karlsruhe, Germany.

Rubinstein, R. and Barton, J. M. (1990): Nonlinear Reynolds Stress Models and the Renormalization Group, Physics of Fluids A 2 (8), pp. 1472-1476.

Shih, T.H., Zhu, J. and Lumley, J.L. (1995): A new Reynolds stress algebraic equation model, Computational Methods in Applied Mechanics and Engineering, Vol. 125, pp. 287-302.

Saad, Y. (2003): Iterative Methods for Sparse Linear System (Second Edition), Society for Industrial & Applied Mathematics.

Salaheldin, T.M., Imran, J. and Chaudhry, M.H. (2004): Numerical modeling of three-dimensional flow field around circular piers, Journal of Hydraulic Engineering, ASCE, Vol. 130, No. 2, pp. 91-100.

van Rijn, L.C. (1993): Principles of Sediment Transport in Rivers, Estuaries and Coastal Seas, Aqua Publications.

Wilson, C.A.M.E., Boxall, J.B., Guymer, I. and Olsen, N.R.B. (2003): Validation of a three-dimensional numerical code in the simulation of pseudo-natural meandering flows, Journal of Hydraulic Engineering, ASCE, Vol. 129, No. 10, pp. 758-768.

Wu, W.M., Rodi, W. and Wenka, T. (2000): 3D numerical modeling of flow and sediment transport in open channels, Journal of Hydraulic Engineering, ASCE, Vol. 126, No. 1, pp. 4-15.

Zhang, H., Nakagawa, H., Ishigaki, T., Muto, Y. and Khaleduzzaman, A.T.M. (2005): Flow and bed deformation around a series of impermeable and permeable spur dykes, Proc. of the international conference on monitoring, prediction and mitigation of water-related disasters (MPMD2005), Jan. 12-15, Kyoto, pp.197-202.

三次元非構造格子を用いたレイノルズ方程の有限体積解法について

張　浩*・中川　一・石垣泰輔**・武藤裕則

*京都大学大学院工学研究科
**関西大学工学部都市環境工学科

要旨

　本研究では，三次元非構造格子を用いたレイノルズ平均ナビエ・ストークス方程式の有限体積解法を示している．異なる格子構造を結合することにより生じるコントロール・ボリュームにおける保存則の問題を，厳密かつ有効なデータ構造とすることで解決する方法を示している．空間差分には指数法が，また時間差分には隠的Crank-Nicolson法が用いられている．表面フラックスの計算にあたっては，チェッカーボード現象を避けるためにRhie-Chowによる補間法を用いている．系を構成する方程式群は，最終的にILUTP 法による前処理を伴ったGMRES法を用いて解かれている．本研究による方法を３種の室内実験流れに対して適用したところ，それらの条件の異なるいずれに対してもほぼ満足な流況を再現することが示された．

キーワード:　三次元，有限体積法，非構造格子，　$k-\varepsilon$ モテル